Optics Letters

Deep neural network-assisted high-accuracy microwave instantaneous frequency measurement with a photonic scanning receiver

Yuewen Zhou, Fangzheng Zhang,* [ID] Jingzhan Shi, [ID] and Shilong Pan [ID]

Key Laboratory of Radar Imaging and Microwave Photonics, Ministry of Education, Nanjing University of Aeronautics and Astronautics, Nanjing 210016, China
Corresponding author: zhangfangzheng@nuaa.edu.cn

A microwave instantaneous frequency measurement system with a photonic scanning receiver is proposed in which deep neural network (DNN)-assisted frequency estimation is used to deal with the system defects and improve the accuracy. The system performs frequency-to-time mapping by optical-domain frequency scanning and electrical-domain intermediate frequency envelop detection. Thanks to the optical frequency multiplication, the system can measure high frequency signals in a large spectral range. The DNN establishes an accurate mapping between the digital samples and real frequencies, based on which high-accuracy measurement is achieved. The measurement of signals from 43 to 52 GHz is experimentally demonstrated. Compared with the direct measurements, the DNN-assisted method achieves obviously reduced average errors of about 3.2 MHz. © 2020 Optical Society of America

https://doi.org/10.1364/OL.391883

Microwave instantaneous frequency measurement (IFM) is used in many fields such as wireless communication and electric warfare [1,2]. As electric systems develop towards much higher operation frequencies, microwave IFM with a broad frequency measurement range is highly demanded. Due to the bandwidth limitations, traditional IFM faces challenges to cover a large frequency measurement range. To address this, many photonic microwave IFM schemes have been proposed [3–6], in which the frequency measurement range can easily cover from the *L* band to Ka band (1–40 GHz). However, many of the photonic microwave IFM systems suffer from a large measurement error of around hundreds of megahertz [6], which is far from the requirements for spectrum sensing. Until now, one of the photonic microwave IFM methods with high accuracy uses a stimulated Brillouin scattering effect in optical fibers, in which the measurement error is less than 20 MHz [7]. Recently, we have proposed an IFM scheme using a photonic scanning receiver implemented by optical-domain frequency scanning and electrical-domain intermediate frequency (IF) envelop detection [8,9]. Based on this principle, microwave frequency measurements from 28 to 37 GHz are demonstrated with a measurement error of less than 15 MHz. In Refs. [8,9], the IFM

is integrated with a radar function, making the design of the system restricted. In this Letter, we present a generalized implementation of this photonic-scanning-receiver-based IFM and emphasize the factors that deteriorate the measurement accuracy. More importantly, a deep neural network (DNN)-assisted method is proposed to deal with the system defects which result in measurement errors. The DNN is a powerful machine learning algorithm capable of approximating arbitrary functions. In recent years, a machine learning technique has been applied in the field of optoelectronics to enhance the system performance [10–14]. In Ref. [10], a convolutional neural network (CNN) is successfully used to enhance the performance of the Brillouin IFM by mapping the estimated frequency to the final result. In this process, digital pre-processing is required to get the estimated frequency before the CNN-based optimization. In this Letter, different from [10], the DNN is used to acquire the frequency of the signal under test (SUT) directly from the sampled digital signals, which simplifies the measurement procedure and leads to a small latency. Besides, feature extraction from the raw data can help to achieve good performance in compensating for the system defects.

Figure 1 shows the schematic diagram of the IFM system and the DNN structure used for extracting the frequency. The continuous-wave (CW) light from a laser diode (LD) is modulated by a Mach–Zehnder modulator (MZM1), which is driven by a linearly frequency modulated (LFM) signal generated by a low-speed electrical signal generator (ESG). The LFM signal is set to have a large power such that high-order modulation sidebands can be generated in the obtained optical signal. After MZM1, an erbium-doped fiber amplifier (EDFA: EDFA1) is used to boost the optical power, and an optical dual-band filter (ODBF) is followed to select the ±*n*th-order (*n* is a positive integer) modulation sidebands. The obtained optical signal (at point a) is expressed as

$$E_1(t) \propto J_n(\alpha)[e^{j2\pi(f_c+nf_{\mathrm{LFM}})t} + e^{j2\pi(f_c-nf_{\mathrm{LFM}})t}], \qquad \textbf{(1)}$$

where $J_n(\cdot)$ is the nth-order Bessel function of the first kind, α is the modulation index, f_c is the frequency of the CW light, and $f_{\mathrm{LFM}} = f_0 + kt$ is the frequency of the LFM signal in a single period ($0 < t \le T$) with T, f_0, and k being the temporal period,
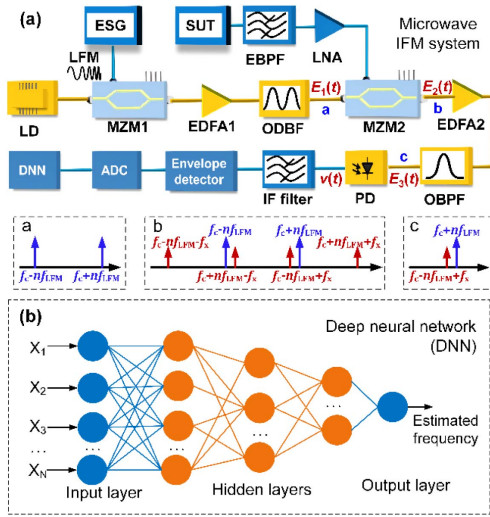
Fig. 1. (a) Schematic diagram of the microwave IFM system and (b) the structure of the DNN.

the initial frequency, and the chirp rate, respectively. It should be noted that when n is an odd number, MZM1 is biased at its minimum transmission point to suppress the optical carrier and even-order modulation sidebands, while MZM1 is biased at the maximum transmission point when n is an even number, to suppress the odd-order modulation sidebands. To avoid spectral aliasing between adjacent sidebands, $n(f_0 + kT) \leq (n + 2) f_0$ should be satisfied, requiring $n \leq 2 f_0 / (kT)$.

The optical signal after ODBF is sent to another MZM (MZM2). The SUT is passed through an electrical bandpass filter (EBPF) and amplified by a low noise amplifier before being applied to drive MZM2. Here the EBPF functions as an image reject filter. The signal after MZM2 (at point b) can be expressed as

$$E_2(t) \propto J_0(\beta) J_n(\alpha)[e^{j2\pi(f_c + n f_{\mathrm{LFM}})t} + e^{j2\pi(f_c - n f_{\mathrm{LFM}})t}]$$

$$+ J_1(\beta) J_n(\alpha)[e^{j2\pi(f_c + n f_{\mathrm{LFM}} + f_x)t} + e^{j2\pi(f_c + n f_{\mathrm{LFM}} - f_x)t}]$$

$$+ J_1(\beta) J_n(\alpha)[e^{j2\pi(f_c - n f_{\mathrm{LFM}} + f_x)t} + e^{j2\pi(f_c - n f_{\mathrm{LFM}} - f_x)t}], \quad \textbf{(2)}$$

where β is the modulation index and f_x is the frequency of the SUT. Here only the $\pm$1st-order modulation sidebands are considered. After MZM2, another EDFA (EDFA2) is used to boost the optical power. Within the expected frequency measurement range of the IFM system, the 1st-order sideband at $f_c - n f_{\mathrm{LFM}} + f_x$ is close to the optical carrier at $f_c + n f_{\mathrm{LFM}}$, and they are selected out by an optical bandpass filter (OBPF). The obtained optical signal (at point c) is

$$E_3(t) \propto J_0(\beta) J_n(\alpha)[e^{j2\pi(f_c + n f_{\mathrm{LFM}})t}]$$

$$+ J_1(\beta) J_n(\alpha)[e^{j2\pi(f_c - n f_{\mathrm{LFM}} + f_x)t}]. \quad \textbf{(3)}$$

Then the optical signal is sent to a photodetector (PD) to perform optical-to-electrical conversion, and the output electrical signal is

$$v(t) \propto J_n{}^2(\alpha) J_0(\beta) J_1(\beta) \cos[2\pi(2n f_{\mathrm{LFM}} - f_x)t]$$

$$+ \tfrac{1}{2} J_n{}^2(\alpha)[J_0{}^2(\beta) + J_1{}^2(\beta)], \quad \textbf{(4)}$$

which contains a direct-current component and a frequency component at $|2n f_{\mathrm{LFM}} - f_x|$. Following the PD, a narrow-band IF filter is applied to select the component at f_{IF}. Mathematically, the spectrum of the obtained signal from is

$$S_E(f) \propto [\delta(f) + \delta(f - |2n f_{\mathrm{LFM}} - f_x|)]\delta(f - f_{\mathrm{IF}})$$

$$= \delta(|2n f_{\mathrm{LFM}} - f_x| - f_{\mathrm{IF}})\delta(f - f_{\mathrm{IF}}), \quad \textbf{(5)}$$

in which $\delta(f) + \delta(f - |2n f_{\mathrm{LFM}} - f_x|)$ is the spectrum of $v(t)$, and $\delta(f - f_{\mathrm{IF}})$ is the transfer function of an ideal narrow-band IF filter. By applying a microwave envelope detector after the IF filter, the envelop of the signal in Eq. (5) is obtained as

$$e(t) = \delta(|2n f_0 + 2nkt - f_x| - f_{\mathrm{IF}})$$

$$= \begin{cases} 1 & t = \frac{f_x + f_{\mathrm{IF}} - 2n f_0}{2nk} \ or \ \frac{f_x - f_{\mathrm{IF}} - 2n f_0}{2nk} \\ 0 & \text{else} \end{cases}. \quad \textbf{(6)}$$

Based on Eq. (6), f_x can be estimated by

$$f_x = 20c\, 2n f_0 + 2nkt_x - f_{\mathrm{IF}}; \ or \ 2n f_0 + 2nkt_x + f_{\mathrm{IF}}, \quad \textbf{(7)}$$

where t_x is the time when $e(t) \neq 0$. This way, the frequency to be measured is mapped to the time position. Through the digital signal sampled by an analog-to-digital converter (ADC), the frequency of the SUT can be estimated. According to Eq. (7), the frequency to be measured should be located in $[2n f_0 - f_{\mathrm{IF}}, \ 2n f_0 - f_{\mathrm{IF}} + 2nkT]$ or $[2n f_0 + f_{\mathrm{IF}}, \ 2n f_0 + f_{\mathrm{IF}} + 2nkT]$. To avoid overlapping between the two spectral ranges, $2nkT \leq 2 f_{\mathrm{IF}}$ should be satisfied. Meanwhile, to eliminate the measurement ambiguity, the image reject filter (EBPF) should have a specific passband within $[2n f_0 - f_{\mathrm{IF}}, 2n f_0 - f_{\mathrm{IF}} + 2nkT]$ or $[2n f_0 + f_{\mathrm{IF}}, 2n f_0 + f_{\mathrm{IF}} + 2nkT]$. The maximum frequency measurement range of this method is $2nkT$, which is $2n$ times of the bandwidth of the input LFM signal. Therefore, the proposed system not only can make the most of current ESGs with high precision and flexibility, but also can considerably expand the operation frequency of current electrical frequency scanning receivers.

In obtaining Eq. (6), the IF filter is assumed to have an ideal response while, in practice, it has a certain bandwidth, and an input single-tone frequency is mapped to a short pulse in a time domain. The pulse width is inversely proportional to the bandwidth of the IF filter [15]. Therefore, the bandwidth of the IF filter should be properly chosen to achieve both a high measurement accuracy and a good measurement resolution [8]. Typically, the full width at half-maximum of the generated pulses is on the level of nanoseconds or even picoseconds. Insufficient sampling rate and precision of the ADC will cause measurement errors. Although the influence of a low sampling rate can be alleviated by appropriate interpolation techniques, the system also suffers from other defects which cannot be easily compensated for. Specifically, these system defects include the nonlinearity during electrical-to-optical and optical-to-electrical conversions, the spontaneous emission noises of the laser and optical amplifiers, the finite out-of-band suppression and edge roll-off of the optical filters, and the unideal wideband frequency responses of the electronic or optoelectronic devices, etc. All these factors would result in measurement errors. To deal with these problems, we propose to use a DNN to extract the frequency information.

Figure 1(b) shows the structure of the DNN we employed, which consists of one input layer, multiple hidden layers, and one output layer. The digital samples in one frequency measurement period are applied as the input, and the output is the estimated frequency of the SUT. The input and output layers are fully connected layers with linear activation functions, and all the hidden layers use the log-sigmoid function as the nonlinear activation function for each neural [16]. The DNN is trained using the digital samples as the input and the corresponding real frequency value as the target. When training the DNN, the network parameters are optimized by minimizing the loss function, which is the mean square error between the output of the DNN and the real frequency value. To avoid overfitting, the Bayesian regularization algorithm is applied [17] during the training process. Once the DNN is optimized, it can be used to estimate the frequency of the SUT. Because the DNN can establish an accurate mapping between the digital waveforms and the instantaneous frequencies, the overall influence of all the system defects can be compensated for.

A proof-of-concept experiment is carried out to investigate the performance of the proposed IFM method. In the experiment, the light generated by an LD (TeraXion Inc.) has a wavelength of 1550.12 nm. The LFM signal generated by an ESG (Tektronix AWG70001A) has a bandwidth of 1.5 GHz (5.5–7 GHz) and a repetition rate of 100 kHz. Both of the MZMs (Fujitsu FTM7938EZ) have a bandwidth of ∼25 GHz. MZM1 is biased at the minimum transmission point. An ODBF realized by a Waveshaper (Finisar Inc.) is used to select the ±3rd-order modulation sidebands ($n = 3$). MZM2 is biased at the quadrature point. The SUT is generated by a microwave signal generator (Agilent, E8257D). Since the image frequency interference is not considered, the EBPF is not used in the experiment. The PD has a bandwidth of 10 GHz, and the IF filter is centered at 10 GHz with a bandwidth of 15 MHz. The optical spectra at different points are monitored by an optical spectrum analyzer with a resolution of 0.02 nm. The electrical signal after the envelop detector is sampled and recorded by a real-time oscilloscope (Agilent, DSO-X 92504A). According to the system parameters, the frequency measurement range is 9 GHz, which is six times that of the bandwidth of the LFM signal. In the experiment, frequency measurements of the SUT from 43 to 52 GHz with a step of 200 MHz are demonstrated.

First, as an example to show the measurement procedure, the frequency of the SUT is set to 46 GHz. The optical spectra of the signals after MZM1 and after the ODBF are shown in Fig. 2(a), in which the ±3rd-order modulation sidebands are successfully selected with the undesired components well suppressed. Figure 2(b) shows the spectra of the signals after MZM2 and after the OBPF. It is found that the signal spectrum after the OBPF agrees well with the expected spectrum at point c in Fig. 1(a). Figure 3 shows the waveform of the envelope signal within a single measurement period of 10 µs, which is captured by the oscilloscope with a sampling rate of 50 MSa/s. As can be seen, a short pulse appears at the time position of 3.32 µs. According to Eq. (7), the frequency of the SUT is estimated to be 45.988 GHz with a measurement error of 12 MHz. Then the frequency of the SUT is tuned from 43 to 52 GHz with a step of 200 MHz. Each frequency is measured for five times, and the average errors at different frequencies are shown in Fig. 4(a). In Fig. 4(a), the measurement errors are kept within 10.8 MHz,
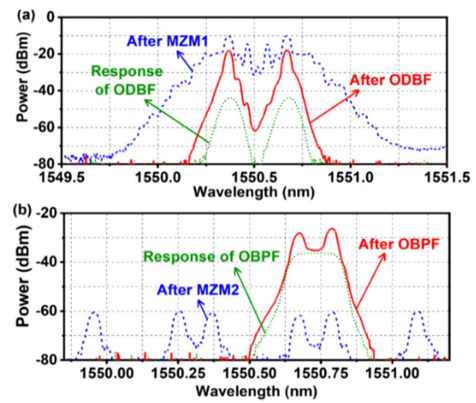

Fig. 2. (a) Optical spectra of the signals after MZM1 and after the ODBF, and (b) the optical spectra of the signals after MZM2 and after the OBPF.
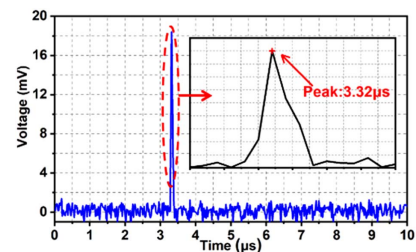

Fig. 3. Waveform of the sampled digital signal when the frequency of the SUT is 46 GHz (sampling rate: 50 MSa/s).
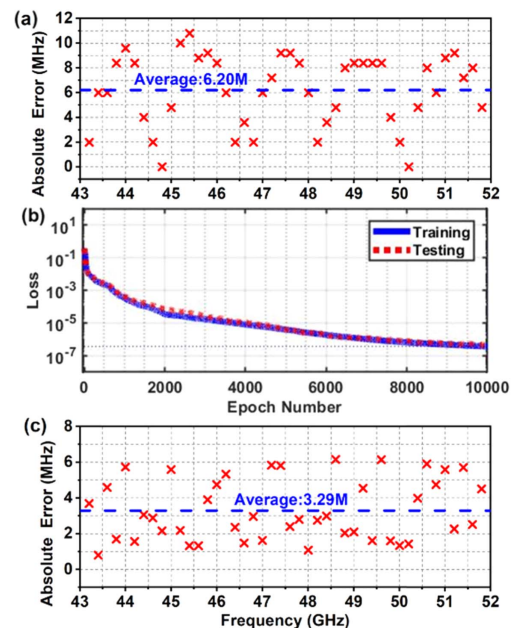

Fig. 4. (a) Average errors by direct measurement, (b) loss curves for training and testing the DNN, and (c) average errors with DNN-assisted frequency estimation.

and the average error considering all the frequencies is calculated to be 6.2 MHz.

Next, DNN-assisted frequency estimation is performed. The data used for training and testing the network are experimentally generated by 500 times measurement at each frequency from 43 to 52 GHz with a step of 200 MHz. For each measurement at different frequencies, the recorded digital waveform in one period and the corresponding real frequency compose one set of data. The DNN is configured to have three hidden layers, and the number of neurons in each hidden layer is set to 500, 50, and 5, respectively. For each frequency, 90 percent of the data are randomly selected to train the network, and the rest are used to test the trained DNN. When training the DNN, the learning rate is set to 0.05, and the epochs are 10000. The training process takes about 30 min using a computer with an Intel i9-9900k CPU (16-core) and an NVIDIA Geforce-RTX-2080Ti GPU. The loss curves for training and testing the DNN are shown in Fig. 4(b), where both the training loss and the testing loss converge to 10^{-6}. Then we use the same digital samples as those in Fig. 4(a) to evaluate the performance of the DNN-assisted frequency estimation. It should be noted that these digital signals are not used for training or testing the DNN. Herein, the latency for a single measurement is about ∼80 μs, which includes a single frequency sweeping period, and the time used for running the DNN. Figure 4(c) shows the absolute measurement errors at different frequencies for the DNN-assisted method. As can be seen, the maximum error is 6.15 MHz, and the mean error considering all the frequencies is 3.29 MHz, both of which are smaller than the result in Fig. 4(a). Therefore, the DNN-assisted frequency estimation achieves much better accuracy.

Finally, the influence of sampling rate of the ADC on the measurement accuracy is investigated. Figure 5 shows the average errors in direct measurement as used for obtaining the result in Fig. 4(a) and the average errors in DNN-assisted measurements, when the sampling rates of the ADC are 25, 30, 40, and 50 MSa/s, respectively. At different sampling rates, the DNN is retrained, and it has the same structure except for the input layer, of which the size is adjusted according to the number of sampling points in a single measurement period. In Fig. 5, when the sampling rate decreases, the average error increases from 6.2 to 12 MHz for the direct measurement method, whereas the average errors of the DNN-assisted measurement are kept around 3.2 MHz. Thus, the DNN-assisted method is applicable to improve the measurement accuracy in variable sampling rates. Besides, by using the DNN-assisted method, the average errors are reduced by 47%, 60%, 69%, and 73%, as the sampling rate decreases. Thus, the advantage of the DNN-assisted method is more prominent for a lower sampling rate. This property indicates the potential of the proposed method for relaxing the hardware requirement. As a comparison, we test the frequency estimation using different interpolation techniques. Figure 5 also shows the average errors when the frequency estimation is done by performing spline interpolation to the sampled digital signals. Here the spline interpolation is chosen, because it achieves slightly better accuracy compared to other interpolation techniques. In Fig. 5, the measurement accuracy by using spline interpolation is still related to the sampling rate, i.e., the error changes from 4.2 to 8.7 MHz as the sampling rate decrease. Although the interpolation method achieves better accuracy compared with the direct measurement method, it still lags behind the DNN-assisted method. This result further confirms that the DNN-assisted method can compensate for all
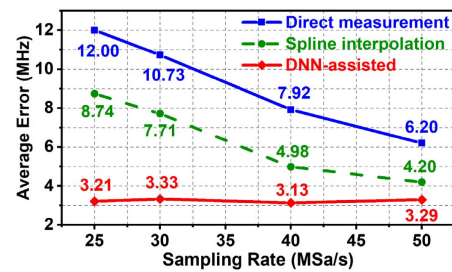

Fig. 5. Average errors in direct measurement, spline-interpolation-based measurement, and DNN-assisted measurement when the ADC has different sampling rates.

the system defects to achieve a higher accuracy, especially for the system with a low sampling rate.

In conclusion, we have demonstrated a DNN-assisted IFM system with a photonic scanning receiver. The system has the capability to measure signals at high frequency and in a large spectral range. The use of DNN for extracting the frequency can obviously enhance the measurement accuracy. The results verify the advantages of the system, which is a good solution to wideband and accurate IFM in wireless communication and electric warfare systems.

Disclosures. The authors declare no conflicts of interest.

REFERENCES

1. P. Ghelfi, F. Scotti, D. Nori, and A. Bogoni, IEEE J. Sel. Top. Quantum Electron. **25**, 1 (2019).
2. P. W. East, IET Radar Sonar Navigat. **6**, 112 (2012).
3. X. Zou, W. Li, W. Pan, L. Yan, and J. Yao, IEEE Trans. Microw. Theory Tech. **61**, 3470 (2013).
4. T. A. Nguyen, E. H. W. Chan, and R. A. Minasian, Opt. Lett. **39**, 2419 (2014).
5. H. Chi, X. Zou, and J. Yao, IEEE Photonics Technol. Lett. **20**, 1249 (2008).
6. J. Shi, F. Zhang, D. Ben, and S. Pan, IEEE Trans. Microw. Theory Tech. **67**, 544 (2018).
7. X. Long, W. Zou, and J. Chen, Opt. Express **25**, 2206 (2017).
8. J. Shi, F. Zhang, X. Ye, Y. Yang, D. Ben, and S. Pan, Opt. Lett. **44**, 1948 (2019).
9. J. Shi, F. Zhang, D. Ben, and S. Pan, J. Lightwave Technol. **38**, 2171 (2020).
10. X. Zou, S. Xu, S. Li, J. Chen, and W. Zou, Opt. Lett. **44**, 5723 (2019).
11. S. Xu, X. Zou, B. Ma, J. Chen, L. Yu, and W. Zou, Light Sci. Appl. **8**, 66 (2019).
12. H. Ye, G. Y. Li, and B. Juang, IEEE Wireless Commun. Lett. **7**, 114 (2018).
13. B. Wang, L. Wang, N. Guo, Z. Zhao, C. Yu, and C. Lu, Opt. Express **27**, 2530 (2019).
14. F. N. Khan, Q. Fan, C. Lu, and A. P. T. Lau, J. Lightwave Technol. **37**, 493 (2019).
15. C. Mittermayer and A. Steininger, IEEE Trans. Instrum. Meas. **48**, 1103 (1999).
16. J. Schmidhuber, Neural Netw. **61**, 85 (2015).
17. F. Burden and D. Winkler, in Artificial Neural Networks: Methods and Applications (2008), Vol. **458**, p. 23.